# *In Vivo Imaging with a Cell-Permeable Porphyrin-Based MRI Contrast*



**Citation:** Lee, Taekwan et al. "In Vivo Imaging with a Cell-Permeable Porphyrin-Based MRI Contrast Agent." Chemistry & Biology 17 (2010): 665-673.

**As Published:** http://dx.doi.org/10.1016/j.chembiol.2010.05.009

**Publisher:** Elsevier B.V.

**Persistent URL:** http://hdl.handle.net/1721.1/66549

**Version:** Author's final manuscript: final author's manuscript post peer review, without publisher's formatting or copy editing

Published in final edited form as:
*Chem Biol*. 2010 June 25; 17(6): 665–673. doi:10.1016/j.chembiol.2010.05.009.

# *In vivo* imaging with a cell-permeable porphyrin-based MRI contrast agent

**Taekwan Lee**[1], **Xiao-an Zhang**[2], **Shanta Dhar**[2], **Henryk Faas**[1], **Stephen J. Lippard**[2,†], and **Alan Jasanoff**[1,3,4,†]

[1] Department of Biological Engineering, Massachusetts Institute of Technology, 150 Albany St., NW14–2213, Cambridge, MA 02139

[2] Department of Chemistry, Massachusetts Institute of Technology, 150 Albany St., NW14–2213, Cambridge, MA 02139

[3] Department of Brain & Cognitive Sciences, Massachusetts Institute of Technology, 150 Albany St., NW14–2213, Cambridge, MA 02139

[4] Department of Nuclear Science & Engineering, Massachusetts Institute of Technology, 150 Albany St., NW14–2213, Cambridge, MA 02139

## SUMMARY

Magnetic resonance imaging (MRI) with molecular probes offers the potential to monitor physiological parameters with comparatively high spatial and temporal resolution in living subjects. For detection of intracellular analytes, construction of cell-permeable imaging agents remains a challenge. Here we show that a porphyrin-based MRI molecular imaging agent, Mn-(DPA-$C_2$)$_2$-$TPPS_3$, effectively penetrates cells and persistently stains living brain tissue in intracranially injected rats. Chromogenicity of the probe permitted direct visualization of its distribution by histology, in addition to MRI. Distribution was concentrated in cell bodies after hippocampal infusion. Mn-(DPA-$C_2$)$_2$-$TPPS_3$ was designed to sense zinc ions, and contrast enhancement was more pronounced in the hippocampus, a zinc-rich brain region, than in the caudate nucleus, which contains relatively little labile $Zn^{2+}$. Membrane permeability, optical activity, and high relaxivity of porphyrin-based contrast agents offer exceptional functionality for *in vivo* imaging.

## INTRODUCTION

Molecular imaging of intracellular targets and processes using magnetic resonance must rely on effective uptake of contrast agents by cells *in vivo*. Small molecule MRI contrast agents are typically based on highly polar, often charged, paramagnetic metal chelates such as Gd-diethylenetriaminetetraacetic acid (DTPA) or Gd-tetraazacyclododecanetetraacetic acid (DOTA), which have intrinsically low transmembrane permeability (Caravan et al., 1999). To reduce barriers against cellular uptake of polar contrast agents, it has been possible to conjugate them to distinct chemical moieties that promote intracellular internalization. Most extensively explored have been so-called cell-penetrating peptides (CPPs) (Derossi et al., 1994; Vives et al., 1997), short polycationic amino acid sequences that transport various

[†]address correspondence to AJ & SJL, jasanoff@mit.edu; lippard@mit.edu.

molecular cargoes into cells (Fonseca et al., 2009). $Gd^{3+}$-containing small molecule MRI contrast agents conjugated to CPPs are effectively internalized by cells *in vitro* (Allen and Meade, 2003; Bhorade et al., 2000; Heckl et al., 2002; Prantner et al., 2003). Further conjugation-based cell delivery approaches have involved fusion of contrast agents to amphipathic moieties (Endres et al., 2006; Sturzu et al., 2009) or thiol-reactive groups (Digilio et al., 2009) that are thought to interact with plasma membrane components. Incorporation of MRI contrast agents into liposomes or carbon nanotubes also facilitates cell delivery (Torchilin, 2007). Few of these approaches have been shown to promote intracellular localization of paramagnetic contrast agents in intact tissue, however.

An alternative approach to producing cell-permeable contrast agents is to construct agents from paramagnetic platforms that intrinsically favor transport into cells. Water soluble metalloporphyrins provide suitable building blocks for this purpose (Zhang et al., 2007). A quintessential porphyrin-based MRI contrast agent, Mn(III)-*meso*-tetrakis(4-sulfonatophenyl)porphyrin (Mn-$TPPS_4$), has high longitudinal ($T_1$) magnetic resonance relaxivity (Chen et al., 1984; Koenig et al., 1987) and localizes in tumors (Fiel et al., 1987; Lyon et al., 1987; Ogan et al., 1987). There is evidence that metalloporphyrin (Megnin et al., 1987) or expanded porphyrin (Woodburn, 2001; Young et al., 1996) agents penetrate cells under various circumstances, possibly because of their hydrophobic surface area and charge delocalization over the aromatic porphyrin ring. Imaging probes based on porphyrins could be designed to target or sense analytes using mechanisms previously applied in conjunction with DTPA or DOTA-related chelates (Jasanoff, 2007).

As an initial test of the metalloporphyrin platform for molecular imaging, we recently synthesized Mn-$(DPA\text{-}C_2)_2$-$TPPS_3$ (Figure 1A), a Mn-$TPPS_4$ analog containing dipicolylamine (DPA) groups to bind labile $Zn^{2+}$ ions (Zhang et al., 2007). Relatively high, 200 μM concentrations of this probe incubated with cultured cells produced robust contrast enhancements. $T_1$-weighted MRI signal increases in cell culture were more pronounced for Mn-$(DPA\text{-}C_2)_2$-$TPPS_3$ than for Mn-$TPPS_4$, and were greatest for the probe in the presence of 1 mM exogenous $Zn^{2+}$ ions. An inconsistency between zinc-dependent MRI changes exhibited by Mn-$(DPA\text{-}C_2)_2$-$TPPS_3$ in cells *vs.* buffer suggested that the cell culture results arose from differences in the relative uptake efficiencies of zinc-complexed and uncomplexed forms of the molecule, rather than from zinc-dependent effects on its relaxivity. Neither the extent of cellular uptake of the probe nor its subcellular localization were directly measured in this study, however.

Based on our *in vitro* results, we speculated that Mn-$(DPA\text{-}C_2)_2$-$TPPS_3$ might be able to function, analogously to histological dyes, as an MRI-detectable stain with both cell permeability and possible zinc dependence in intact animals. Such a function would require that cellular uptake be able to compete kinetically with elimination of the probe following its infusion or injection into tissue. In an organism, both post-infusion concentrations of the probe and the accessible concentrations of labile zinc would most likely be far below those we applied in cell culture, so uptake and zinc binding would be less favorable. To assess the behavior of Mn-$(DPA\text{-}C_2)_2$-$TPPS_3$ in a true biological environment, we therefore applied the contrast agent by injection into live rodent brains, where cell-permeable analyte-sensitive molecular imaging agents could be particularly important for monitoring neurobiological function and disease. We here provide compelling evidence of intracellular probe localization *in vivo*, as well as indications of zinc sensitivity, which suggest the general utility of the porphyrin platform for further applications.

# RESULTS

## Mn-(DPA-$C_2$)$_2$-TPPS$_3$ produces strong, persistent contrast in injected brains

To assess the ability of Mn-(DPA-$C_2$)$_2$-TPPS$_3$ to penetrate cells and stain living brain tissue, 5 μL of a 1 mM solution of the probe were injected intracranially into the dorsal hippocampus of rat subjects. Each infusion was paired with a symmetric 5 μL injection of 1 mM Mn-TPPS$_4$ into the contralateral hemisphere, and anesthetized animals were subsequently imaged on a 9.4 T MRI scanner. The paired injection procedure was designed to test whether relative staining patterns observed with the two agents *in vitro* would be reproduced *in vivo*, while at the same time controlling for trial-to-trial variability in experimental parameters such as animal positioning and radiofrequency coil tuning. Injected rats were examined at multiple time points following contrast agent delivery. After two days, strong contrast was consistently observed in the hippocampus injected with Mn-(DPA-$C_2$)$_2$-TPPS$_3$, whereas little signal enhancement over background was observed on the side injected with Mn-TPPS$_4$ (Figure 1B). This result demonstrates that the relatively efficient cellular contrast induction exhibited by Mn-(DPA-$C_2$)$_2$-TPPS$_3$ *in vitro* is reproduced in living brain tissue.

Rats were scanned again at four and ten days after contrast agent injection. Contrast differences between Mn-(DPA-$C_2$)$_2$-TPPS$_3$ and Mn-TPPS$_4$ injection sites remained throughout this period (Figure 1C). MRI signal was quantified in regions of interest (ROIs) around the injection sites. Each ROI was defined by a 1.2 mm radius sphere centered around an injection site, as judged from images with isotropic 150 μm resolution. Measured signal amplitudes were normalized with respect to control ROIs near but outside the injected areas. Examination of the MRI signal time courses graphed in Figure 1D shows that the signal difference between Mn-(DPA-$C_2$)$_2$-TPPS$_3$ and Mn-TPPS$_4$ injection areas decayed to approximately half its initial value over the ten day observation period, suggesting an approximately half-life of 10 days for injected Mn-(DPA-$C_2$)$_2$-TPPS$_3$. A mean maximal enhancement of 21 ± 7% ($n$ = 7) with respect to the control volume was observed in the Mn-(DPA-$C_2$)$_2$-TPPS$_3$ infusion ROI, whereas average MRI signal in the Mn-TPPS$_4$ region was slightly less intense with respect to the control, probably because of signal dropout in the immediate vicinity of the injection needle insertion site. Signal differences between Mn-(DPA-$C_2$)$_2$-TPPS$_3$ and Mn-TPPS$_4$ ROIs were statistically significant on all days ($t$-test $p$ = 0.006–0.027).

Persistence of the MRI signal enhancement produced by Mn-(DPA-$C_2$)$_2$-TPPS$_3$ over several days suggested that this probe was sequestered intracellularly or tightly bound to immobilized components of the tissue. To better understand the contrasting dynamics of signal changes caused by Mn-TPPS$_4$, the time course of image enhancement was examined over a short time scale following Mn-TPPS$_4$ injection in two further animals. Image series (see Figure S1) showed that $T_1$-weighted contrast enhancement occurred shortly after delivery of Mn-TPPS$_4$, but that the signal increase dissipated almost entirely over a period of less than two hours. Fast clearance from brain has been observed previously with classical hydrophilic MRI contrast agents such as Gd-DTPA (Liu et al., 2004; Wan et al., 1991), which are thought to have a predominantly extracellular tissue distribution.

## Porphyrin-based probe localizes to cell bodies in the hippocampus

The spatial pattern of the contrast enhancement observed with Mn-(DPA-$C_2$)$_2$-TPPS$_3$ was examined at a microanatomical level. Comparison of MRI and Nissl-stained histological images (Figure 2A–B) revealed strong similarities and suggested that the most hyperintense regions resolved by MRI corresponded to RNA-rich structures, probably cell somata. Systematic differences between MRI enhancements observed in the three hippocampal

subfields, CA1, CA3, and dentate gyrus (DG), were not discernable. Further analysis of localization patterns was aided by the optical absorbance of Mn-(DPA-$C_2$)$_2$-$TPPS_3$. In particular, 100 μm sections of injected rat brains extracted after imaging displayed intrinsic contrast resulting from the probe and directly reflecting its distribution in the brain. Close-up views of a representative section (Figure 2C–D) displayed a yellow-brown color that appeared most concentrated in laminae that were also strongly stained by the nuclear stain 4′,6-diamidino-2-phenylindole (DAPI; Figure 2E–F). These results imply that MRI contrast enhancement in brain regions injected with Mn-(DPA-$C_2$)$_2$-$TPPS_3$ was largely due to localization of the probe in cell bodies.

The intrinsic optical contrast due to injected probe was relatively homogeneous in 100 μm sections (Figure 2D), suggesting that Mn-(DPA-$C_2$)$_2$-$TPPS_3$ was broadly distributed in intracellular compartments. In addition, near the injection needle insertion points, discrete darker colored spheroids of approximately 5 μm in diameter were observed under bright-field illumination of 30 μm sections (Figure 3). Some of these spheroids corresponded to structures also resolved by terminal deoxynucleotidyl transferase-mediated dUTP nick end labeling (TUNEL staining, Fig. 3E–F). MRI hyperintense areas more distal from the injection sites did not exhibit TUNEL positivity. We therefore infer that the brown TUNEL-positive puncta might be cells that had been physically disrupted by the injection procedure and that had acquired particularly high concentrations of the contrast agent. Based on the absence of TUNEL-positive cells and the normal appearance of Nissl staining throughout most of the MRI contrast-enhanced brain regions, we conclude that the probe had little deleterious effect on brain tissue in general, and is therefore unlikely to be strongly cytotoxic. We also noted no serious changes to the behavior of injected rats in the home cage environment, which provides further indication that contrast agent delivery is not significantly harmful to the animals, despite its relatively long retention time in the brain.

### Mn-(DPA-$C_2$)$_2$-$TPPS_3$ retained in brain tissue is primarily cytosolic

The accumulation of Mn-(DPA-$C_2$)$_2$-$TPPS_3$ in injected brain tissue was examined directly by trace element analysis. Rats received bilateral hippocampal infusions of 5 μL contrast agent ($n$ = 6) or phosphate buffered saline (PBS) vehicle control ($n$ = 6), and were scanned after two days. Immediately after MRI, these animals were sacrificed and dissected to obtain dorsal hippocampal tissue specimens weighing an average of 28.8 ± 1.7 mg (wet weight), each containing much of the volume of distribution around an injection site. Samples were digested, dried, and evaluated by flameless atomic absorption spectroscopy (AAS) to determine the amounts of manganese present. Excess manganese in test samples versus PBS controls was taken to reflect the local deposition of Mn- (DPA-$C_2$)$_2$-$TPPS_3$. The mean Mn concentrations in test and control samples were 2.5 ± 0.5 and 0.44 ± 0.03 parts per million (ppm = μg/g wet tissue), respectively. The difference of 2.1 ppm is equivalent to approximately 40 μM contrast agent, assuming brain density of 1 g/mL, a dilution of the infusate by a factor of 25 that presumably reflects convective dynamics during the injection, diffusion and wash-out during the two day post-infusion period, and aspects of sample preparation. Manganese concentrations from AAS correlated closely ($R$ = 0.87, $p < 0.0001$) with MRI intensities measured from 1.2 mm-radius spherical ROIs around the infusion sites (Figure 4A). The regression coefficient of 10.7% MRI signal change per ppm Mn was combined with a reference $T_1$ measurement from rat hippocampus (de Graaf et al., 2006) to estimate an "*in vivo* relaxivity" of about 3 $mM^{-1}s^{-1}$ for injected Mn-(DPA-$C_2$)$_2$-$TPPS_3$. This approximate value is somewhat lower, but of the same order of magnitude, as the reported relaxivity range of 6.7–8.7 $mM^{-1}s^{-1}$ of the contrast agent in buffer at 4.7 T (Zhang et al., 2007). These results provide absolute evidence of probe accumulation in injected tissue and validate AAS as a basis for semi-quantitative estimates of the Mn-(DPA-$C_2$)$_2$-$TPPS_3$ concentrations that gave rise to observed MRI contrast enhancements.

The AAS analysis was extended to provide information about the subcellular distribution of injected Mn-(DPA-$C_2$)$_2$-$TPPS_3$. Brain samples from an additional set of animals injected with either Mn-(DPA-$C_2$)$_2$-$TPPS_3$ or PBS were combined ($n$ = 4 per condition), homogenized, and fractionated to determine the manganese content in cytosolic, nuclear, and mixed membranous compartments of the tissue (Cox and Emili, 2006). Figure 4B shows the manganese concentrations measured by AAS in each of the three fractions. Total Mn concentrations summed across the three intracellular fractions were lower than the average values measured from unfractionated samples, a disparity which we presume to reflect primarily differences in sample preparation techniques. The fact that similar, approximately twofold, discrepancies were found in both test and control samples argues against the possibility that a particularly large amount of extracellular contrast agent was present in the samples injected with Mn-(DPA-$C_2$)$_2$-$TPPS_3$. Data from the fractionated samples indicate that the cytosol contained 69% of the manganese found near Mn-(DPA-$C_2$)$_2$-$TPPS_3$ injection sites, and 66% of the excess manganese observed with respect to control injections. Nuclear and membranous fractions contained 14% and 21% of the excess Mn, respectively. The AAS data therefore demonstrate conclusively that the injected probe entered cells, and suggest that the contrast patterns observed by MRI arose largely from cytosolically-localized Mn-(DPA-$C_2$)$_2$-$TPPS_3$.

### Mn-(DPA-$C_2$)$_2$-$TPPS_3$ stains a zinc-rich brain area with greater efficiency

In addition to exploiting cell permeability of the porphyrin platform, Mn-(DPA-$C_2$)$_2$-$TPPS_3$ was designed to respond to labile zinc ions; the probe exhibits zinc-dependent MRI contrast enhancement in cells *in vitro* (Zhang et al., 2007). To begin examining zinc sensitivity of Mn-(DPA-$C_2$)$_2$-$TPPS_3$ *in vivo*, we compared contrast due to probe injection into two brain structures known to contain differing levels of labile zinc. Areas of the hippocampus are consistently identified as some of the most $Zn^{2+}$-rich neural structures in mammals (Nakashima and Dyck, 2009). Reservoirs of vesicular $Zn^{2+}$ have been associated with glutamatergic synaptic transmission and may play a role in hippocampal long term potentiation (Frederickson et al., 2005). Although technical limitations of the injection procedure prevented us from performing a meaningful analysis of relative Mn-(DPA-$C_2$)$_2$-$TPPS_3$ staining in hippocampal sub-regions, we examined whether MRI-visualized Mn-(DPA-$C_2$)$_2$-$TPPS_3$ staining in the hippocampus was more pronounced than staining in the caudate-putamen, a region of the basal ganglia shown by histochemical analyses to contain substantially less labile $Zn^{2+}$ (Frederickson et al., 1987; Frederickson et al., 1992).

As in the hippocampus, Mn-(DPA-$C_2$)$_2$-$TPPS_3$ produced clear contrast enhancement in the caudate, whereas Mn-$TPPS_4$ did not (Figure 5A). Contrast observed in the caudate was relatively featureless by comparison to enhancements observed in the hippocampus however, possibly reflecting the absence of cytoarchitectonic laminae in this structure. In addition, markedly greater MRI signal was observed following Mn-(DPA-$C_2$)$_2$-$TPPS_3$ injection into the hippocampus than into the caudate-putamen area (Figure 5B). Across six animals injected in both sites, probe injections resulted on average in a 19.5 ± 8.5% signal increase with respect to uninjected control ROIs in the hippocampus, but only a 4.2 ± 2.0% increase in the caudate. In both brain regions, differences between the signal changes produced by Mn-(DPA-$C_2$)$_2$-$TPPS_3$ and Mn-$TPPS_4$ injection were statistically significant ($t$-test $p$ = 0.02–0.04), but the mean difference observed in the hippocampus (24 ± 10%) was over threefold higher than in the caudate (7.1 ± 4.1%). The previously reported weak zinc dependence of Mn-(DPA-$C_2$)$_2$-$TPPS_3$ relaxivity in solution (Zhang et al., 2007) could not explain the results and would have predicted a lower MRI intensity in the hippocampus with respect to the caudate. The measurements instead support the conclusion that accumulation of Mn-(DPA-$C_2$)$_2$-$TPPS_3$ was more pronounced in the hippocampus than in the caudate

nucleus, consistent with the hypothesis that this probe accumulates more efficiently in brain areas that contain greater amounts of labile $Zn^{2+}$.

To examine further the relationship between *in vivo* staining and $Zn^{2+}$ availability, we combined hippocampal injection of Mn-(DPA-$C_2$)$_2$-$TPPS_3$ with pretreatment using the high-affinity zinc chelator tris(2-pyridylmethyl)amine (TPA; XZ and SJL, unpublished results). A 4 μL dose of 1 mM TPA or vehicle was delivered to sites in opposite hemispheres, followed by 4 μL of 1 mM probe. The relative MRI signal averaged across hippocampal ROIs in all animals was 124 ± 8% without TPA and 109 ± 12% with TPA. Although the difference is not statistically significant (*t*-test $p = 0.3$, $n = 5$), the lower image intensity observed in the presence of TPA is compatible with the explanation that TPA-mediated $Zn^{2+}$ chelation reduced uptake of the probe, within the limits of experimental variability across the tested animals.

## DISCUSSION

### Advantages of metalloporphyrin-based agents for *in vivo* molecular imaging

Results presented here highlight the advantages of metalloporphyrin-based MRI contrast agents for molecular imaging *in vivo*. The first is cell permeability, a property for which earlier *in vitro* experiments with Mn-(DPA-$C_2$)$_2$-$TPPS_3$ provided only circumstantial evidence (Zhang et al., 2007). In rat brains, the contrast agent proved to stain cells persistently and with significantly greater efficiency than its more polar parent molecule, Mn-$TPPS_4$. The observed pattern of contrast enhancement with Mn-(DPA-$C_2$)$_2$-$TPPS_3$ suggests that the probe most effectively stains neuronal cell bodies, as opposed to plexiform layers. Correspondence between MRI intensity enhancement and the intrinsic contrast of the probe in brain sections indicates that preferential staining of gray matter was due directly to accumulation of Mn-(DPA-$C_2$)$_2$-$TPPS_3$, rather than to differences in apparent relaxivity of the probe in white and gray matter. The bias for gray matter is also consistent with AAS results showing robust accumulation of Mn-(DPA-$C_2$)$_2$-$TPPS_3$ in cytosol. The data presented here demonstrate that Mn-(DPA-$C_2$)$_2$-$TPPS_3$ entered cells in intact brain tissue, rather than merely partitioning into membranes or other hydrophobic environments. This behavior indicates that the metalloporphyrin platform should be well suited to the construction of cell-permeable molecular imaging agents for MRI.

A second advantage of the metalloporphyrin platform for molecular imaging is the potential for multimodal measurements with porphyrin-based probes. In the study that presented synthesis of Mn-(DPA-$C_2$)$_2$-$TPPS_3$, we noted that the apoporphyrin form of this agent exhibits zinc-dependent fluorescence (Zhang et al., 2007). Here we used the optical absorbance of Mn-(DPA-$C_2$)$_2$-$TPPS_3$ itself to determine the distribution of the probe in post-mortem brain slices. Given the possibility, sometimes by design, that environmental factors can influence MRI signal enhancement by a contrast agent, the ability to map porphyrin-based probe distribution by this optical method is an extremely important asset. In addition to facilitating quantitative interpretation of molecular imaging results, the optical assay can help localize probes on length scales below the resolution of MRI. Combined MRI and histological analysis is of obvious value for experiments in laboratory animals, and a similar approach could also be useful for studies relating MRI contrast enhancement to biopsy samples in a clinical diagnostic context.

### Zinc sensing via accumulation of an MRI contrast agent

Mn-(DPA-$C_2$)$_2$-$TPPS_3$ displayed evidence of zinc sensitivity in injected rat brains. Contrast enhancement was substantially more pronounced in the labile zinc-rich hippocampus than in the caudate nucleus, which contains much less vesicular $Zn^{2+}$. If labile zinc were the only

factor that determined localization patterns of Mn-(DPA-$C_2$)$_2$-$TPPS_3$ in the brain, the MRI results presented here would have matched previously reported fluorescent and histochemical maps of zinc distribution (Frederickson, 2003; Frederickson et al., 2000). Results from these *ex vivo* techniques have shown relatively light staining in the caudate-putamen (Frederickson et al., 1987; Frederickson et al., 1992), but intense and specific layer- and subfield-dependent staining patterns in the hippocampus, especially emphasizing the mossy fiber pathway from DG to CA3 (Slomianka, 1992). Such precise results were not obtained by MRI, possibly in part because of the tendency of the probe to accumulate in cells even in the absence of zinc (Zhang et al., 2007), perhaps compounded by disruptions following from the injection procedure itself. There was no evidence for extensive cell disruption or death, however, so cytotoxicity is unlikely to have been a major factor in the results. Zinc detection with Mn-(DPA-$C_2$)$_2$-$TPPS_3$ or related compounds could be improved in the future by modifying the probe further to disfavor zinc-independent staining, and by using experimental paradigms that involve less invasive, more homogeneous probe delivery methods.

Zinc-dependent contributions to the tissue accumulation of Mn-(DPA-$C_2$)$_2$-$TPPS_3$ may have arisen in part because of charge-related effects. Mn-(DPA-$C_2$)$_2$-$TPPS_3$ is anionic (−2) in the absence of analyte, but neutral or cationic (+2) when bound to one or two $Zn^{2+}$ ions, respectively. Neutral or positively charged species are thought to be more readily imported by cells. Mn-$TPPS_4$ is even more negatively charged (−3) than Mn-(DPA-$C_2$)$_2$-$TPPS_3$, which may account for its relatively fast elimination from injected brain tissue. The idea of generating contrast based on analyte-dependent transport of a molecular imaging agent has parallels to a variety of MRI-based tracer techniques (Lin and Koretsky, 1997; Mansson et al., 2006; Querol and Bogdanov, 2006), but represents a sharp departure from ion-sensitive MRI contrast mechanisms based on $T_1$ or $T_2$ relaxivity changes (Atanasijevic et al., 2006; Atanasijevic et al., 2010; Esqueda et al., 2009; Li et al., 1999; Que and Chang, 2009). Molecular transport *in vivo* is inherently complex, as well as irreversible on a short time scale, but analyte sensing based on transport of an agent might nevertheless have advantages over detection based on relaxivity changes. In particular, transport-based probes could achieve greater MRI signal changes, both because of the possibility that their accumulation might be facilitated by relatively small amounts of analyte (in analogy to ionophores and transmembrane carrier proteins, for instance), and because relatively high contrast could be developed during extended probe infusion protocols. Owing to their cell permeability and ability to induce robust contrast changes in living tissue, paramagnetic metalloporphyrins may prove to be effective platforms on which to improve and diversify probe localization-based approaches to measuring biological targets *in vivo*.

## SIGNIFICANCE

Results presented here demonstrate that a paramagnetic metalloporphyrin MRI molecular imaging agent penetrates cells in tissue and permits analysis of neural structures in living mammalian brains, without apparent toxic side effects. Imaging agents based on intrinsically membrane-permeable platforms like porphryins constitute an effective alternative to probes formed by conjugating contrast agents to specific cell delivery vehicles. Optical absorbance of the probe employed here, Mn-(DPA-$C_2$)$_2$-$TPPS_3$, allowed MRI contrast results to be validated by conventional post-mortem histology, illustrating a further advantage of porphyrin-based agents. Mn-(DPA-$C_2$)$_2$-$TPPS_3$ binds $Zn^{2+}$ ions with high affinity (Zhang et al., 2007), and preliminary evidence of zinc-dependent uptake of the probe was provided by comparison of staining results obtained in brain regions containing different labile zinc concentrations. MRI-based molecular imaging with probes that accumulate in analyte-dependent fashion *in vivo* represents a novel and potentially generalizable approach distinct from strategies for sensing analytes via relaxivity changes.

# EXPERIMENTAL PROCEDURES

## MRI contrast agents

Mn-(DPA-$C_2$)$_2$-$TPPS_3$ was prepared and purified as previously described (Zhang et al., 2007). Mn-$TPPS_4$ was purchased from Frontier Scientific (Logan, UT). Both Mn- (DPA-$C_2$)$_2$-$TPPS_3$ and Mn-$TPPS_4$ were dissolved into phosphate buffered saline (PBS) to constitute 1 mM solutions for infusion experiments.

## Animal subjects

Male Lewis rats (250–300 g) were purchased from Charles River Laboratories (Wilmington, MA). After arrival, animals were housed and maintained on a 12 hour light/dark cycle and permitted *ad libitum* access to food and water. All procedures were performed in strict compliance with the Committee on Animal Care (CAC) guidelines of Massachusetts Institute of Technology.

## Contrast agent infusion

Animals were anesthetized with isoflurane (4% induction, 1–2% maintenance), shaved, and mounted in a rodent stereotaxic device (David Kopf Instruments, Tujunga CA) prior to surgery. Heart rate and blood oxygenation were continuously monitored using a pulse oximeter (Nonin Medical, Plymouth, MN) during subsequent procedures. The scalp was retracted and small holes were drilled into the skull above desired injection sites. 28G needles (Plastics One, Roanoke, VA) were lowered to the appropriate depth through the holes. Infusion coordinates were defined with reference to a standard atlas (Paxinos and Watson, 1998), as follows: 3 mm posterior, 2 mm lateral, and 3.4 mm ventral to bregma for the hippocampus, and 0.5 mm posterior, 3 mm lateral, and 5 mm ventral to bregma for the caudate nucleus. At each injection site, 5 μL of either Mn-(DPA-$C_2$)$_2$-$TPPS_3$ or Mn-$TPPS_4$ was infused using an injection pump (Cole-Parmer, Vernon Hills, IL) operating with an infusion rate of 18 μL/h. For several experiments, an injection of 4 μL 1 mM TPA (ATRP Solutions, Pittsburgh, PA) preceded infusion of 4 μL contrast agent. TPA was dissolved to 100 mM in dimethyl sulfoxide (DMSO) and diluted to 1 mM in PBS; vehicle controls were 1% DMSO in PBS. After each infusion, the injection needle was held in place for five minutes to prevent reflux before withdrawing. The scalp was sutured and in some cases animals were scanned while still under surgical anesthesia. Further imaging experiments were conducted after recovery of the animals. Experiments in which conditions were paired (Mn-(DPA-$C_2$)$_2$-$TPPS_3$ *vs.* Mn-$TPPS_4$ or +TPA *vs.* −TPA), brain hemispheres exposed to each given condition were alternated.

## Magnetic resonance imaging

MRI scans were obtained up to ten days post-injection. Animals were anesthetized with 1–2% isoflurane and mounted into a positioning device under a four-channel phased array radiofrequency coil (Bruker Biospin, Billerica, MA). The animal holder was inserted into a 20 cm bore 9.4 T magnet operated from a Bruker Biospec console, and animals were monitored with a respirometer (Bruker Biospin). Data were acquired with a $T_1$-weighted gradient echo pulse sequence and an acceleration factor of two, with 48 reference lines for multichannel data reconstruction. Images with 150 μm cubic voxel size were obtained with a repetition time (*TR*) of 50 ms, echo time (*TE*) of 6 ms, field of view (FOV) of 30 × 30 × 22.5 mm, and data matrix of 200 × 200 × 150 points (no averaging, scan time = 15.5 min); images with 75 × 75 × 300 μm voxel size were obtained with *TR* = 50 ms, *TE* = 6 ms, FOV = 30 × 30 × 150 mm, and data matrix of 400 × 400 × 50 points (4-fold averaging, scan time = 37.3 min).

### Image analysis

Images were reconstructed in Paravision 4 (Bruker Biospin) and transformed to AFNI data format; data conversion and further image processing were performed using AFNI (Cox, 1996). Brains were segmented away from non-brain matter and ROIs were defined as spheres of 1.2 mm radius around injection sites identified in the images. Mean signal intensity in each ROI was computed by averaging over voxels. Signal in each ROI was normalized by the mean signal recorded in an uninjected control region with the same dorsoventral and rostrocaudal coordinates as the injection site. Control regions had equivalent size to the injected ROIs and were located in primary or secondary somatosensory cortex, paired with hippocampal or caudate injection sites, respectively. Local normalization by signal in the control regions served to eliminate systematic effects of image inhomogeneity on the measured signal intensities. Statistical analyses and further data display were performed using Excel (Microsoft, Redmond, WA) and Kaleidagraph (Synergy Software, Reading, PA). Unless otherwise noted, error margins reported in the text reflect standard errors of the mean (s.e.m.) over multiple measurements.

### Histology

After the final scanning sessions, rats were sacrificed by isoflurane overdose and perfused with PBS, followed by 4% buffered formaldehyde solution. Brains were removed and stored in 4% formaldehyde for several days. Thin brain slices (40 μm for Nissl staining and 30 μm for TUNEL staining) were cut with a Leica VT1200 microtome (Leica Microsystems, Wetzlar, Germany). For Nissl staining, brain slices were mounted on gelatin coated slides (SouthernBiotech Associates, Birmingham, AL) and stained with cresyl violet following a common procedure (Paxinos and Watson, 1998). For TUNEL staining, brain slices were rinsed twice with PBS and dried on the gelatin coated slides. Mounted slices were processed with 50 μL TUNEL reaction solution supplied as part of the Roche Applied Science (Mannheim, Germany) In Situ Death Detection Kit, TMR red. After one hour of incubation at 37°C, brain slices were rinsed three times with PBS and treated with mounting medium including DAPI (Vector Laboratories, Burlingame, CA). Photomicrographs from these slides were acquired using an Olympus BX50WI epi-fluorescence microscope (Olympus America, Center Valley, PA) equipped with a Spot RT741 digital camera (Diagnostic Instruments, Sterling Heights, MI).

### Trace element analysis

For analysis of manganese content in injected rat hippocampus, 12 animals were infused bilaterally with 5 μL of 1 mM Mn-(DPA-$C_2$)$_2$-$TPPS_3$ or PBS vehicle control solutions and scanned after two days with 150 μm isotropic resolution, using methods described above. Immediately after MRI, these rats were sacrificed and decapitated. Brains were quickly removed and dorsal hippocampal segments were dissected. Brain samples were immediately placed on dry ice and stored in a −80 °C freezer. Twenty-four samples weighing 16–47 mg and containing the injection volumes were analyzed to determine total manganese content. Tissue samples were processed according to a published protocol (Pera and Harder, 1977), beginning with digestion in nitric acid at 40 °C, followed by evaporation to near dryness. Dried, digested samples were resuspended in 1 N HCl (2 mL) and again heated to near dryness; this procedure was repeated twice. Dried samples were finally dissolved in 1 mL 0.1 N HCl for manganese analysis by flameless atomic absorption spectrophotometry (AAS). Measurements were performed on an AAnalyst 600 instrument from Perkin-Elmer (Waltham, MA). Calibration was performed using manganese aqueous standards prepared in 5% nitric acid from a commercial standard solution (Perkin-Elmer Pure AS Standard). The calibration curve for Mn was linear over the range from 1–200 μg/L, and the mean Mn concentration determined from vehicle control samples (0.44 ± 0.09 ppm) was comparable to a published precedent (Cosan et al., 2006).

Eight additional hippocampal samples weighing 19–36 mg were analyzed to determine the distribution of manganese among cytosolic, nuclear, and mixed membranous fractions. Brain specimens were fractionated following a published procedure (Cox and Emili, 2006). Briefly, tissue samples were weighed and washed with ice-cold 250-STMDPS buffer [50 mM Tris-HCl, pH 7.4, 250 mM sucrose, 5 mM $MgCl_2$, 1 mM dithiothreitol (DTT), 1 mM phenylmethanesulfonyl fluoride (PMSF), 25 μg/mL spermine, and 25 μg/mL spermidine] and then submerged in 250-STMDPS buffer. After 15 strokes in a Dounce homogenizer, the extract was centrifuged at 800*g* for 15 min and the pellet was used to prepare the nuclear fraction. The 800*g* supernatant was centrifuged again at 100,000*g* in a swinging-bucket ultracentrifuge for 1 h. The supernatant from this separation constituted the cytosolic fraction; the remaining sedimented material was further processed to isolate membrane-containing components. The pellet was resuspended in 0.5 mL of membrane extraction buffer (20 mM Tris-HCl, pH 7.8, 0.4 M NaCl, 15% glycerol, 1 mM DTT, 1 mM PMSF and 1.5% Triton-X-100) and incubated for 1 h with gentle rocking, followed by centrifugation for 30 min at 9,000*g*. The membranous fraction (plasma membrane, Golgi bodies, vesicles, endoplasmic reticulum) was considered to be the supernatant from this separation. The pellet was homogenized with a single stroke in a Dounce homogenizer in 2M-TMDPS buffer (50 mM Tris–HCl, pH 7.4, 2 M sucrose, 5 mM $MgCl_2$, 1 mM DTT, 1mM PMSF, 25 μg/mL spermine, and 25 μg/mL spermidine) and further fractionated at 8,000*g* for 35 min. The pellet from this final centrifugation was resuspended in nuclear extraction buffer (20 mM HEPES, pH 7.9, 1.5 mM $MgCl_2$, 0.5 M NaCl, 0.2 mM EDTA and 20%, glycerol) and used as the nuclear fraction. Manganese concentrations in all fractions were determined by AAS, as described above.

### *In vivo* relaxivity estimation

Relaxivity of Mn-(DPA-$C_2$)$_2$-$TPPS_3$ in injected rat brain was estimated using the approximation that $r_1 \approx (\Delta I/I)(\Delta c)^{-1}(T_1)^{-1}$, which is valid under strong $T_1$-weighting conditions like those applied here ($TR$ = 50 ms), where $r_1$ is the longitudinal relaxivity, $\Delta I/I$ is the fractional MRI signal change for a given difference in probe concentration $\Delta c$, and $T_1$ is the initial longitudinal relaxation time. $(\Delta I/I)(\Delta c)^{-1}$ was given by the slope of a linear fit to the plot of AAS measurements *vs.* MRI signal enhancements (Figure 4A): 10.7% MRI signal change per ppm Mn, equivalent to 5.88 fractional MRI change per mM. A $T_1$ value of 2.06 s for rat hippocampus at 9.4 T was obtained from the literature (de Graaf et al., 2006).

## Supplementary Material

Refer to Web version on PubMed Central for supplementary material.

## Acknowledgments

This work was funded by NIH grant DP2-OD2441 (New Innovator Award) and Department of Defense grant DAMD17-03-1-0413 to AJ, and by NIH grant R01-GM65519 to SJL. Additional support was provided by a grant from the McGovern Institute Neurotechnology Program to AJ and SJL.

## Abbreviations

| | |
|---|---|
| **DAPI** | 4′,6-diamidino-2-phenylindole |
| **DG** | dentate gyrus |
| **DPA** | dipicolylamine |
| **FOV** | field of view |
| **Gd-DTPA** | Gd-diethylenetriaminetetraacetic acid |

| | |
|---|---|
| **Gd-DOTA** | Gd-tetraazacyclododecanetetraacetic acid |
| **Mn-TPPS$_4$** | Mn(III)-*meso*-tetrakis(4-sulfonatophenyl)porphyrin |
| **MRI** | magnetic resonance imaging |
| **ROI** | region of interest |
| ***TE*** | echo time |
| **TPA** | tris(2-pyridylmethyl)amine |
| ***TR*** | repetition time |
| **TUNEL** | terminal deoxynucleotidyl transferase-mediated dUTP nick end labeling |

## References


Allen MJ, Meade TJ. Synthesis and visualization of a membrane-permeable MRI contrast agent. J Biol Inorg Chem. 2003; 8:746–750. [PubMed: 14505078]

Atanasijevic T, Shusteff M, Fam P, Jasanoff A. Calcium-sensitive MRI contrast agents based on superparamagnetic iron oxide nanoparticles and calmodulin. Proc Natl Acad Sci U S A. 2006; 103:14707–14712. [PubMed: 17003117]

Atanasijevic T, Zhang XA, Lippard SJ, Jasanoff A. MRI Sensing Based on the Displacement of Paramagnetic Ions from Chelated Complexes. Inorg Chem. 2010; 49:2589–91. [PubMed: 20141114]

Bhorade R, Weissleder R, Nakakoshi T, Moore A, Tung CH. Macrocyclic chelators with paramagnetic cations are internalized into mammalian cells via a HIV-tat derived membrane translocation peptide. Bioconjug Chem. 2000; 11:301–305. [PubMed: 10821645]

Caravan P, Ellison JJ, McMurry TJ, Lauffer RB. Gadolinium(III) chelates as MRI contrast agents: structure, dynamics, and applications. Chem Rev. 1999; 99:2293–2352. [PubMed: 11749483]

Chen CW, Cohen JS, Myers CE, Sohn M. Paramagnetic metalloporphyrins as potential contrast agents in NMR imaging. FEBS Lett. 1984; 168:70–74. [PubMed: 6705923]

Cosan TE, Demir TA, Yayla E, Cosan D, Berber A, Kaynak Z. Trace minerals in experimental subarachnoid haemorrhage: zinc, copper and manganese levels in rat brain tissue, blood and urine. Acta Neurochir (Wien). 2006; 148:443–448. [PubMed: 16475018]

Cox B, Emili A. Tissue subcellular fractionation and protein extraction for use in mass-spectrometry-based proteomics. Nat Protoc. 2006; 1:1872–1878. [PubMed: 17487171]

Cox RW. AFNI: software for analysis and visualization of functional magnetic resonance neuroimages. Comput Biomed Res. 1996; 29:162–173. [PubMed: 8812068]

de Graaf RA, Brown PB, McIntyre S, Nixon TW, Behar KL, Rothman DL. High magnetic field water and metabolite proton T1 and T2 relaxation in rat brain in vivo. Magn Reson Med. 2006; 56:386–394. [PubMed: 16767752]

Derossi D, Joliot AH, Chassaing G, Prochiantz A. The third helix of the Antennapedia homeodomain translocates through biological membranes. J Biol Chem. 1994; 269:10444–10450. [PubMed: 8144628]

Digilio G, Catanzaro V, Fedeli F, Gianolio E, Menchise V, Napolitano R, Gringeri C, Aime S. Targeting exofacial protein thiols with Gd(III) complexes. An efficient procedure for MRI cell labelling. Chem Commun (Camb). 2009:893–895. [PubMed: 19214307]

Endres PJ, Macrenaris KW, Vogt S, Allen MJ, Meade TJ. Quantitative imaging of cell-permeable magnetic resonance contrast agents using x-ray fluorescence. Mol Imaging. 2006; 5:485–497. [PubMed: 17150161]

Esqueda AC, Lopez JA, Andreu-de-Riquer G, Alvarado-Monzon JC, Ratnakar J, Lubag AJ, Sherry AD, De Leon-Rodriguez LM. A new gadolinium-based MRI zinc sensor. J Am Chem Soc. 2009; 131:11387–11391. [PubMed: 19630391]

Fiel RJ, Button TM, Gilani S, Mark EH, Musser DA, Henkelman RM, Bronskill MJ, van Heteren JG. Proton relaxation enhancement by manganese(III)$TPPS_4$ in a model tumor system. Magn Reson Imaging. 1987; 5:149–156. [PubMed: 3586881]

Fonseca SB, Pereira MP, Kelley SO. Recent advances in the use of cell-penetrating peptides for medical and biological applications. Adv Drug Deliv Rev. 2009; 61:953–964. [PubMed: 19538995]

Frederickson C. Imaging zinc: old and new tools. Sci STKE 2003. 2003:pe18.

Frederickson CJ, Kasarskis EJ, Ringo D, Frederickson RE. A quinoline fluorescence method for visualizing and assaying the histochemically reactive zinc (bouton zinc) in the brain. J Neurosci Methods. 1987; 20:91–103. [PubMed: 3600033]

Frederickson CJ, Koh JY, Bush AI. The neurobiology of zinc in health and disease. Nat Rev Neurosci. 2005; 6:449–462. [PubMed: 15891778]

Frederickson CJ, Rampy BA, Reamy-Rampy S, Howell GA. Distribution of histochemically reactive zinc in the forebrain of the rat. J Chem Neuroanat. 1992; 5:521–530. [PubMed: 1476668]

Frederickson CJ, Suh SW, Silva D, Thompson RB. Importance of zinc in the central nervous system: the zinc-containing neuron. J Nutr. 2000; 130:1471S–1483S. [PubMed: 10801962]

Heckl S, Debus J, Jenne J, Pipkorn R, Waldeck W, Spring H, Rastert R, von der Lieth CW, Braun K. CNN-Gd(3+) enables cell nucleus molecular imaging of prostate cancer cells: the last 600 nm. Cancer Res. 2002; 62:7018–7024. [PubMed: 12460922]

Jasanoff A. MRI contrast agents for functional molecular imaging of brain activity. Curr Opin Neurobiol. 2007; 17:593–600. [PubMed: 18093824]

Koenig SH, Brown RD 3rd, Spiller M. The anomalous relaxivity of $Mn^{3+}$($TPPS_4$). Magn Reson Med. 1987; 4:252–260. [PubMed: 3574059]

Li W, Fraser SE, Meade TJ. A calcium-sensitive magnetic resonance imaging contrast agent. J Am Chem Soc. 1999; 121:1413–1414.

Lin YJ, Koretsky AP. Manganese ion enhances T1-weighted MRI during brain activation: an approach to direct imaging of brain function. Magn Reson Med. 1997; 38:378–388. [PubMed: 9339438]

Liu CH, D'Arceuil HE, de Crespigny AJ. Direct CSF injection of $MnCl_2$ for dynamic manganese-enhanced MRI. Magn Reson Med. 2004; 51:978–987. [PubMed: 15122680]

Lyon RC, Faustino PJ, Cohen JS, Katz A, Mornex F, Colcher D, Baglin C, Koenig SH, Hambright P. Tissue distribution and stability of metalloporphyrin MRI contrast agents. Magn Reson Med. 1987; 4:24–33. [PubMed: 3821476]

Mansson S, Johansson E, Magnusson P, Chai CM, Hansson G, Petersson JS, Stahlberg F, Golman K. $^{13}C$ imaging-a new diagnostic platform. Eur Radiol. 2006; 16:57–67. [PubMed: 16402256]

Megnin F, Faustino PJ, Lyon RC, Lelkes PI, Cohen JS. Studies on the mechanism of selective retention of porphyrins and metalloporphyrins by cancer cells. Biochim Biophys Acta. 1987; 929:173–181. [PubMed: 3593779]

Nakashima AS, Dyck RH. Zinc and cortical plasticity. Brain Res Rev. 2009; 59:347–373. [PubMed: 19026685]

Ogan MD, Revel D, Brasch RC. Metalloporphyrin contrast enhancement of tumors in magnetic resonance imaging. A study of human carcinoma, lymphoma, and fibrosarcoma in mice. Invest Radiol. 1987; 22:822–828. [PubMed: 3429177]

Paxinos, G.; Watson, C. The Rat Brain in Stereotaxic Coordinates. 4. New York: Academic Press; 1998.

Pera MF Jr, Harder HC. Analysis for platinum in biological material by flameless atomic absorption spectrometry. Clin Chem. 1977; 23:1245–1249. [PubMed: 872370]

Prantner AM, Sharma V, Garbow JR, Piwnica-Worms D. Synthesis and characterization of a Gd-DOTA-D-permeation peptide for magnetic resonance relaxation enhancement of intracellular targets. Mol Imaging. 2003; 2:333–341. [PubMed: 14717332]

Que EL, Chang CJ. Responsive magnetic resonance imaging contrast agents as chemical sensors for metals in biology and medicine. Chem Soc Rev. 2009; 39:51–60. [PubMed: 20023836]

Querol M, Bogdanov A Jr. Amplification strategies in MR imaging: activation and accumulation of sensing contrast agents (SCAs). J Magn Reson Imaging. 2006; 24:971–982. [PubMed: 17024658]

Slomianka L. Neurons of origin of zinc-containing pathways and the distribution of zinc-containing boutons in the hippocampal region of the rat. Neuroscience. 1992; 48:325–352. [PubMed: 1376449]

Sturzu A, Klose U, Echner H, Beck A, Gharabaghi A, Kalbacher H, Heckl S. Cellular uptake of cationic gadolinium-DOTA peptide conjugates with and without N-terminal myristoylation. Amino Acids. 2009; 37:249–255. [PubMed: 18633572]

Torchilin VP. Targeted pharmaceutical nanocarriers for cancer therapy and imaging. AAPS J. 2007; 9:E128–147. [PubMed: 17614355]

Vives E, Brodin P, Lebleu B. A truncated HIV-1 Tat protein basic domain rapidly translocates through the plasma membrane and accumulates in the cell nucleus. J Biol Chem. 1997; 272:16010–16017. [PubMed: 9188504]

Wan XM, Fu TC, Smith PH, Brainard JR, London RE. Magnetic resonance imaging study of the rat cerebral ventricular system utilizing intracerebrally administered contrast agents. Magn Reson Med. 1991; 21:97–106. [PubMed: 1943681]

Woodburn KW. Intracellular localization of the radiation enhancer motexafin gadolinium using interferometric Fourier fluorescence microscopy. J Pharmacol Exp Ther. 2001; 297:888–894. [PubMed: 11356908]

Young SW, Qing F, Harriman A, Sessler JL, Dow WC, Mody TD, Hemmi GW, Hao Y, Miller RA. Gadolinium(III) texaphyrin: a tumor selective radiation sensitizer that is detectable by MRI. Proc Natl Acad Sci U S A. 1996; 93:6610–6615. [PubMed: 8692865]

Zhang XA, Lovejoy KS, Jasanoff A, Lippard SJ. Water-soluble porphyrins as a dual-function molecular imaging platform for MRI and fluorescence zinc sensing. Proc Natl Acad Sci U S A. 2007; 104:10780–10785. [PubMed: 17578918]

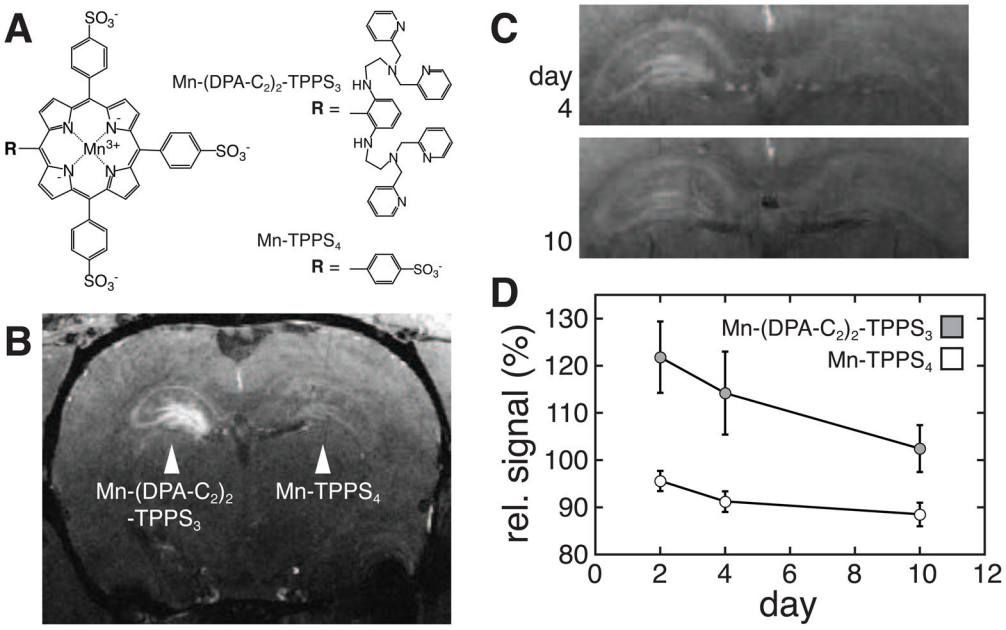


**Figure 1. MRI contrast enhanced by injection of porphyrin agents into rat hippocampus**

(A) Structures of Mn-(DPA-$C_2$)$_2$-$TPPS_3$ and Mn-$TPPS_4$. (B) Contrast enhancement in a representative animal, two days after injection with Mn-(DPA-$C_2$)$_2$-$TPPS_3$ into the left hippocampus and Mn-$TPPS_4$ into the opposite hemisphere. $T_1$-weighted MRI data were acquired with 75 × 75 × 300 μm voxels and *TE*/*TR* = 6/50 ms. (C) Images from the animal in panel (B) obtained four and ten days after injection, showing slowly fading image enhancement near the Mn-(DPA-$C_2$)$_2$-$TPPS_3$ infusion site. (D) A graph of relative MRI signal as a function of time in 1.2 mm-radius spherical regions of interest (ROIs) around the Mn-(DPA-$C_2$)$_2$-$TPPS_3$ and Mn-$TPPS_4$ injection locations. To compute relative MRI signal, the image intensity in each hippocampal ROI was normalized by the signal in uninjected control volumes positioned lateral to the infusion sites. Error bars denote standard errors of the mean (s.e.m.) over 7 rats. See also Figure S1.

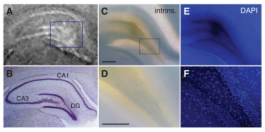


**Figure 2. Microanatomical localization of hippocampal MRI contrast after Mn-(DPA-$C_2$)$_2$-$TPPS_3$ infusion**

(A) Close up of MRI contrast enhancement in injected hippocampus, with Nissl-stained section (B) for comparison. The most hyperintense areas in panel A correlate with dense Nissl-stained cell body layers in panel B. Hippocampal subfields, CA1, CA3, and dentate gyrus (DG), are labeled in B for reference. (C) Intrinsic staining visualized by transmitted light through a 100 μm section obtained from the subject imaged for panels A and B. The field of view centers on the DG and corresponds to the blue rectangle in A. Scale bar = 100 μm. (D) Close up of the area delineated by the dashed rectangle in C, showing homogeneous yellow-brown staining in laminae of DG. Scale bar = 50 μm. (E–F) Visualization of nuclei via DAPI fluorescence in the same section shown in panels C–D (equivalent fields of view).

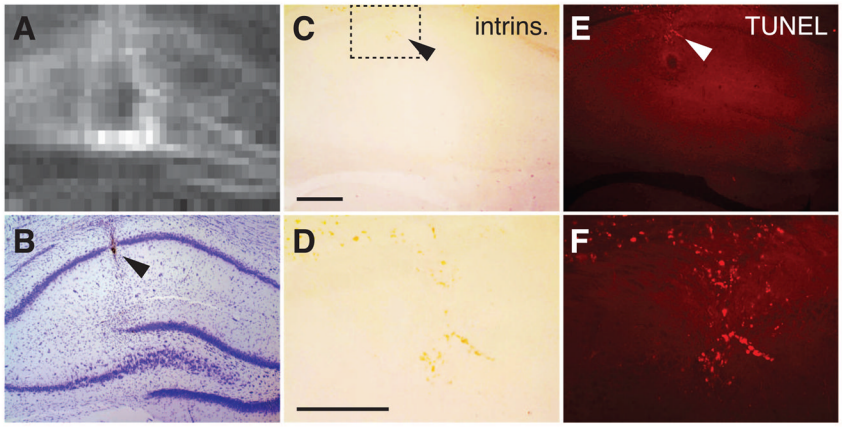


**Figure 3. Foci of contrast agent accumulation and TUNEL positivity near an injection site**

(A) MRI scan showing contrast enhancement around the injection site in another rat infused with Mn-(DPA-$C_2$)$_2$-$TPPS_3$ in the left hippocampus. (B) Nissl stained section corresponding to panel A, showing mechanical damage due to the needle insertion (arrowhead). (C) Intrinsic staining in a bright field view of a 30 μm section corresponding to panels A–B, showing discrete puncta of coloration due to accumulation of the contrast agent in the immediate proximity of the injection needle insertion site (arrowhead). Scale bar = 100 μm. (D) Close up of the view in panel C, corresponding to the dotted rectangle. Scale bar = 50 μm. (E) TUNEL staining to visualize dead cells in the slice shown in panel C. TUNEL positivity is observed only near the needle insertion site (arrowhead), but not in the rest of the section, despite broad MRI contrast enhancement observed throughout the depicted region (*cf.* panel A). (F) Close up of panel E, showing close correspondence of TUNEL-positive foci to colored puncta shown in panel D.

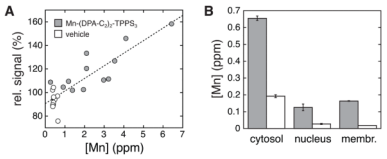


**Figure 4. Quantification of manganese content in injected brain specimens**

(A) Correspondence of manganese concentrations determined by atomic absorption spectroscopy (AAS) with relative image signal determined by MRI for hippocampal specimens injected with Mn-(DPA-$C_2$)$_2$-$TPPS_3$ (gray symbols, $n$ = 12) or PBS vehicle control (white symbols, $n$ = 12). [Mn] values are expressed in parts per million (ppm = μg/g wet tissue), and relative MRI signal was determined as described in the caption to Figure 1. A linear fit to the data gave rise to the dashed line, which has a slope of 10.7% signal change per ppm Mn. The regression was highly significant with $R$ = 0.87 and $p$ < 0.0001. (B) Hippocampal specimens injected with either Mn-(DPA-$C_2$)$_2$-$TPPS_3$ or PBS (each $n$ = 4) were combined, homogenized, and fractionated to determine the concentration of manganese in cytosolic, nuclear, and mixed membranous compartments of the tissue. [Mn] values for each fraction were determined by AAS for test (gray) and control (white) samples, and show primarily cytosolic localization of the contrast agent. Error bars denote standard deviations of three measurements from each sample.

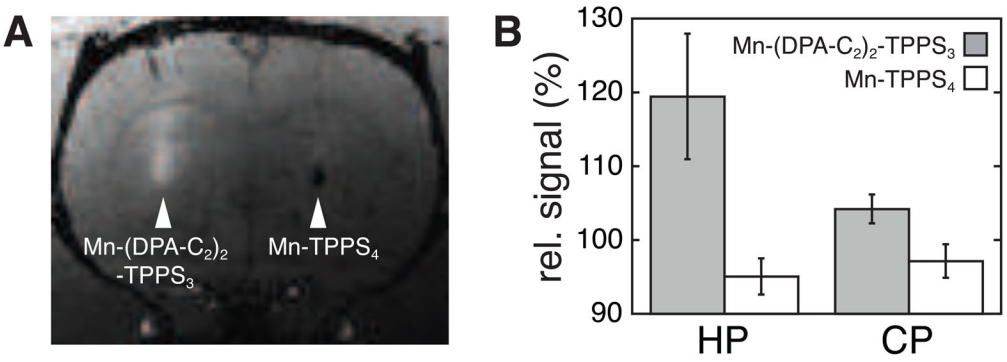


**Figure 5. Differential staining with Mn-(DPA-$C_2$)$_2$-$TPPS_3$ in hippocampus and caudate-putamen**

(A) MRI contrast visualized two days after injection of Mn-(DPA-$C_2$)$_2$-$TPPS_3$ and Mn-$TPPS_4$, respectively, into the left and right caudate-putamen of a representative rat. The image was obtained with 150 μm cubic voxels and *TE*/*TR* = 6/50 ms. (B) As a preliminary test of zinc-dependent uptake of Mn-(DPA-$C_2$)$_2$-$TPPS_3$ in injected brains, relative MRI signal was quantified in hippocampal (HP) and caudate (CP) regions of interest, near injection sites for Mn-(DPA-$C_2$)$_2$-$TPPS_3$ (gray) and Mn-$TPPS_4$ (white). Both brain regions show significantly greater staining with Mn-(DPA-$C_2$)$_2$-$TPPS_3$ than with the control compound, but the difference is roughly three times greater on average in the zinc-rich hippocampus than in the caudate, which contains substantially less labile zinc. Error bars denote s.e.m for $n$ = 6.